Size optimization of organic nanoparticles with aggregation-induced emission characteristics for improved ROS generation and photodynamic cancer cell ablation

Shengming Gan[1], Wenbo Wu[2,3], Guangxue Feng[1,*], Zhiming Wang[1,*], Bin Liu[2,*], Ben Zhong Tang[1, 4,*]

[1] State Key Laboratory of Luminescent Materials and Devices, Guangdong Provincial Key Laboratory of Luminescence from Molecular Aggregates, AIE Institute, South China University of Technology, Guangzhou 510640, China.

[2] Department of Chemical and Biomolecular Engineering, National University of Singapore, 4 Engineering Drive 4, 117585, Singapore

[3] Institute of Molecular Aggregation Science, Tianjin University, Tianjin, 300072, China

[4] School of Science and Engineering, Shenzhen Institute of Molecular Aggregate Science and Technology, The Chinese University of Hong Kong, Shenzhen, 2001 Longxiang Boulevard, Longgang District, Shenzhen, Guangdong 518172, China

*Email: fenggx@scut.edu.cn, wangzhiming@scut.edu.cn, cheliub@nus.edu.sg and tangbenz@cuhk.edu.cn

Abstract

Aggregation-induced emission (AIE) fluorogens provide new opportunities to promote efficient ROS production in aggregates, which represent the promising candidates to construct theranostic nanoparticles for photodynamic therapy (PDT), but the size effect has been rarely explored. Herein, we report a universal method to fabricate organic nanoparticles with controllable sizes and demonstrate that ~45 nm is the optimal size of AIE nanoparticles for PDT. Different from conventional Ce6 nanoparticles which show largely reduced fluorescence and ROS generation efficiency when increasing nanoparticle sizes, AIE nanoparticles show gradually enhanced brightness and ROS generation efficiency upon increasing nanoparticle sizes from 6 nm to ~45 nm. While further increasing sizes could continue intensifying the nanoparticle's brightness at the expense of ROS production, with the optimal size for ROS generation efficiency achieved at ~45 nm. Both 2D monolayer cell and 3D multicellular spheroid experiments further confirm that 45 nm AIE nanoparticles have the highest cellular uptake, deepest penetration depth, and the best photodynamic killing effect. Such study not only manifests the advantages of AIE photosensitizers, but also delivers the optimal size ranging for efficient PDT, which shall provide an attractive paradigm to guide the development of phototheranostic nanoparticles besides molecular design to further promote the PDT applications.

1. Introduction

Photodynamic therapy (PDT) as a new non-invasive treatment method has attracted great attentions in cancer therapy. PDT capitalizes on light-absorbing photosensitizers (PSs) to generate reactive oxygen species (ROS) to cause cancer cell apoptosis and death.[1] Based on the types of generated ROS, PDT can be categorized into two groups. Type II PDT relies on the energy transfer from excited PSs to triplet oxygen to generate singlet oxygen ($^1O_2$), while type I PDT is based on the electron transfer from PSs to surrounding oxygen or substrates to generate free radicals (superoxide anions, hydroxyl radicals, etc.).[2-4] Benefited from the localized light irradiation and the short action radius and lifetime of ROS, PDT holds the unique merits of precise spatiotemporal control, minimal invasiveness, high therapeutic specificity, and so forth.[5, 6] To deliver PSs to tumor area, one of the most adapted strategies is to encapsulate PSs into water-dispersible nanoparticles, which not only improves the biocompatibility of PSs but also renders them the tumor targeting ability through enhanced permeability and retention (EPR) effect and surface-decorated targeting moieties.[7-9] However, most of the traditional PSs such as porphyrins[10], cyanine[11, 12], BODIPY derivatives[13], etc. have planner π-conjugated structures, which tend to form compact aggregates with strong π-π stacking interactions when being encapsulated into nanoparticles. Such π-π stacking results in aggregation-caused quenching (ACQ) effect and leads to largely reduced fluorescence and ROS generation, which greatly compromises their imaging sensitivity and PDT performance.[14-17] Great efforts have been made to fight against ACQ effects, such as reducing PS loading percentage, introducing intraparticle spacers, decorating PS at nanoparticle surface, etc.,[18-20] but with limited success as it has to fight against naturally happened aggregation processes.

Fluorogens with aggregation-induced emission (AIE) characteristics are a new emerging class of optical materials, which showed negligible or weak emission in molecular state but exhibited largely intensified emission in aggregate state or solid state.[21-23] Since its first coinage in 2001, AIE has demonstrated great promising in biological and biomedical applications, ranging from tumor imaging, cell tracking, image-guided surgery, etc.[24-26] Recently, AIE photosensitizers have been reported, which showed brighter fluorescence emission and stronger ROS generation efficiency than traditional PSs in the aggregate state, especially when being encapsulated into nanoparticles, representing one of the most attractive candidates for PDT in recently years.[27-30] However, the progresses of AIE PSs have mainly focused on molecular design such as donor-acceptor engineering or polymerization, while less has been explored on how nanoparticle formation would affect their PDT performance.[31-34] Recently, Ding et al. reported that corannulene-decorated PEG was a better encapsulation

matrix as compared to lipid-PEG to synchronously enhance fluorescence and ROS production of AIE PSs by creating a more compact and rigid interior microenvironment.[35] We also demonstrated that silica shell was favorable for enhancing fluorescence while polymer shells could promote ROS production.[36] However, the influence of nanoparticle sizes on the optical properties especially ROS generation of PSs has been rarely explored, nevertheless to mention its influence on PDT performance due to the difficulties in controlling sizes of pure organic nanoparticles.

Herein, we report a facile strategy to fabricate AIE nanoparticles with controllable sizes and revealed the optimal nanoparticle size of AIE PSs for PDT. Two AIEgens (TPEDC and PTEPDC) and a commercially available ACQ PS (Ce6) were used for nanoparticle formation. Using the modified nano-precipitation method with DSPE-PEG$_{2000}$ as the matrix, a series of nanoparticles with sizes ranging from sub-10 nm to ~100 nm were prepared by changing the feed ratios or solvent-to-water ratios. Both AIE nanoparticles showed gradually enhanced fluorescence along with increased nanoparticle sizes, while their ROS generation efficiency increased firstly and then decreased with the best performance occurred at the nanoparticle sizes of ~35-45 nm. On the contrary, both the fluorescence intensity and ROS production efficiency of Ce6 nanoparticles gradually decreased as the size increased. Such findings not only manifest the advantages of AIE PSs for phototheranostic nanoparticle engineering, but also deliver the optimal size ranging for efficient PDT (Scheme 1). AIE conjugated polymer PTPEDC nanoparticles with the highest ROS production were further decorated with cell penetration peptide (Tat) for evaluation of the photodynamic killing performance. 45 nm PTPEDC-Tat nanoparticles showed the highest cellular uptake while too large or too small nanoparticle showed reduced cellular internalization. In addition, 45 nm PTPEDC-Tat nanoparticles also showed the best penetration depth and best photodynamic cell killing effect in 3D multicellular spheroid experiment. Hence, our study reveals that the ROS generation efficiency and cellular uptake of photosensitizer-loaded organic nanoparticles are size-dependent and the best PDT performance for AIE nanoparticles was achieved at sizes of 35-45 nm. Such comprehensive study shall provide an attractive paradigm to guide the development of phototheranostic nanoparticles beside molecular design to further promote the PDT applications.

Scheme 1. Schematic illustration of size-dependent fluorescence, ROS generation efficiency, and cellular uptake of AIE or ACQ PS-loaded organic nanoparticles for PDT.

2. Results and Discussion

2.1 Photophysical properties of PSs

Figure 1. (a) Chemical structures of PTPEDC, TPEDC and Ce6. AIE titration curves of PTPEDC (b), TPEDC (d) and Ce6 (f) in THF/water mixtures with different water volume fractions. Fluorescence intensity changes of PTPEDC (c), TPEDC (e), and Ce6 (g) along with

increased water fractions, I_0 is the emission intensity in pure THF solution, I is the fluorescence intensity at different water fractions.

To develop pure organic nanoparticles for PDT, one small AIE molecule TPEDC and its corresponding conjugated polymer PTPEDC (M_w = 14269, polydispersity index = 1.71) were synthesized according to literature (Figure 1a), [31] and their structures were confirmed by NMR and high-resolution mass spectroscopy (Figures S1-S4). A commercially available Ce6 with planar cyclic tetrapyrrole structures was also selected for comparison. The optical properties of these three PSs were firstly evaluated by UV-vis and PL spectroscopy. Both TPEDC and PTPEDC showed broad absorption band ranging from 280 nm to 500 nm, and a similar emission maximum centered at 610 nm, respectively. The absorption and emission maxima of Ce6 are located at 666 nm and 673 nm, respectively (Figure S5). Their AIE properties were further investigated by measuring their emission changes in THF/water mixture with varied water fractions. As shown in Figure 1d and 1b, both TPEDC and PTPEDC showed very weak fluorescence in pure THF solution as they are in single molecular state, and the active intramolecular motions dissipate the excited energy via non-radiative decay pathway. Along with increasing water fractions, the emission intensity showed gradual enhancement, which reached the maximum at f_w = 99%, demonstrating obvious AIE properties. Moreover, the higher I/I_0 for PTPEDC as compared to TPEDC indicates the better AIE feature for the conjugated polymers, which shall be attributed to its higher hydrophobicity and more compact aggregation than small molecular counterpart in aqueous solution (Figure 1c and 1e). As the intramolecular movement of the AIE unit in the polymer can be further restricted by the steric hindrance of the backbone and side chains, resulting in high fluorescence efficiency and high sensitivity, AIE polymer PTPEDC has more advantages than AIE small molecules TPEDC in the biological application. On the contrary, Ce6 with planar structure showed largely reduced fluorescence along with increasing water fractions (Figure 1f and 1g). Its fluorescence intensity in water is only one-fifth of that in molecular state, clearly indicating that Ce6 is a typical ACQ fluorophore.

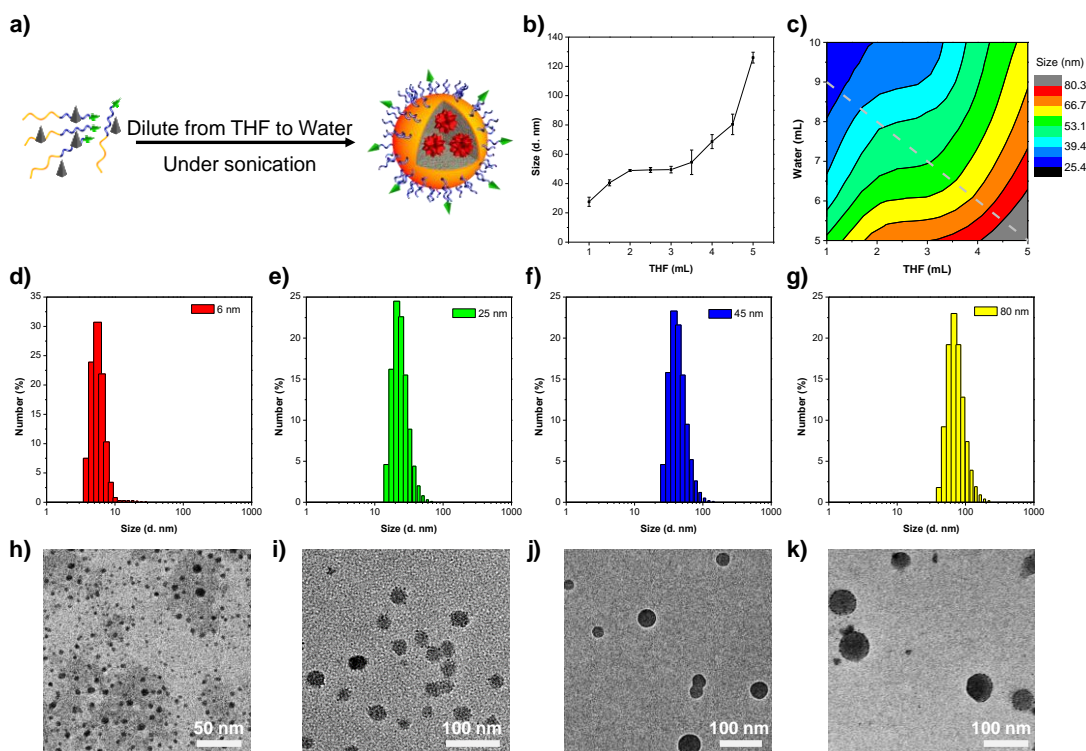## 2.2 Synthesis of pure organic nanoparticles with controllable sizes

Figure 2. (a) Schematic illustration of AIE nanoparticle formation by the nanoprecipitation method. (b, c) The size changes of PTPEDC nanoparticles under different THF to water ratios. Particle size distributions (d-g) and TEM images (h-k) of PTPEDC nanoparticles with sizes of 6 nm (d, h), 25 nm (e, i), 45 nm (f, j) and 80 nm (g, k), respectively. Data presented means ± standard deviation (SD), *n* = 3.

A modified nanoprecipitation method is developed for synthesizing nanoparticles with different sizes. Amphiphilic copolymer, 1,2-distearoyl-sn-glycero-3-phosphoethanolamine-N-[methoxy (polyethylene glycol)-2000] (DSPE-PEG$_{2000}$) with excellent biocompatibility was selected as the encapsulation matrix to load these PSs into the interior of nanoparticles. The nanoparticles were formed upon transferring the good solvent (e.g., THF) that contained PSs and DSPE-PEG$_{2000}$ into the poor solvent (e.g., Milli-Q water) under ultrasound sonication (Figure 2a). In this process, the hydrophobic PSs and DSPE segment intertwined with each other to form the agglomerates, while the hydrophilic polyethylene glycol formed a protective shell to avoid further agglomeration. After THF volatilization, uniformly dispersed nanoparticles aqueous solution was obtained. Nanoparticles with different sizes were fabricated by changing the PS to DSPE-PEG$_{2000}$ feed ratio or THF to water volume ratio. PTPEDC was selected as the model to demonstrate the feasibility of such strategy. Upon fixing the amount of PTPEDC (0.5 mg), DSPE-PEG$_{2000}$ (1 mg) and the total volume of THF and water (10 mL), increasing THF volume leads to enlarged nanoparticles. In details, the nanoparticle sizes increased from ~25 nm to ~126 nm upon increasing THF volume from 1 mL to 5 mL, respectively (Figure 2b).

In a typical nanoparticle formation process, it will undergo initial nucleation, coalescence or agglomeration, and stabilization.[37] A faster nucleation rate and slower agglomeration rate is beneficial for smaller nanoparticles as it provides sufficient time for PEG stabilization.[38, 39] Increasing THF volume will reduce the diffusion rate of PTPEDC and DSPE-PEG$_{2000}$ from THF to water, resulting in a slower nucleation rate, and hence increases the sizes of the formed agglomerates, which eventually leads to larger PTPEDC nanoparticles. A comprehensive set of varied THF and water volumes were also used to prepare PTPEDC nanoparticles. As shown in Figure 2c, either increasing THF volume or decreasing water volume will eventually lead to increased nanoparticle sizes. The nanoparticle sizes could be precisely controlled from ~25 nm to over ~100 nm. However, nanoparticles with sizes smaller than 20 nm could not be obtained under such feed ratios and PTPEDC initial concentration. The reason might be due to the relatively high PTPEDC initial concentration and high PTPEDC to DSPE-PEG$_{2000}$ feed ratio, which could not reduce the agglomeration rate to provide sufficient time for DSPE-PEG$_{2000}$ coating to stabilize these small nanoparticles. To prepare nanoparticles with sub-20 nm and even sub-10 nm sizes, a much smaller PTPEDC to DSPE-PEG$_{2000}$ ratio (1:20 and 1:30), a smaller PTPEDC amount (0.1 mg) and a smaller THF-to-water ratio (1:10) was employed with the help of ultrasound sonication. As a slow THF evaporation rate could lead to the redissolve of small nanoparticles and growth of large agglomerates, rotary evaporator was also used to increase THF evaporation rate immediately after ultrasound sonication (Figure S6).[40] With such modification, PTPEDC nanoparticles with sizes of 6 nm and 20 nm were also obtained.

Eventually, PTPEDC nanoparticles with sizes ranging from 6 nm to above 100 nm were successfully fabricated. High-resolution TEM images were further obtained to verify their sizes and morphologies. As shown in Figure 2h-k, all these PTPEDC nanoparticles are spherical in shapes with high uniformity. The sizes measured from TEM images are in consistence with their hydrodynamic sizes measured from DLS experiments (Figure 2d-g). In addition, slightly increased negative surface zeta potentials were observed along with increased nanoparticle sizes, which shall be caused by the presence of more PEG chains for larger nanoparticles (Figure S7). The sizes of these PTPEDC nanoparticles after being stored in a refrigerator at 4 °C for 6 months were further measured by DLS (Figure S8). The results showed that there was almost no change in size after 6 months, indicating the excellent colloidal stability of the prepared nanoparticles, independent of sizes. With the same method and slightly modified experiment parameters, we have also successfully obtained TPEDC nanoparticles and Ce6 nanoparticles with the sizes ranging from sub-10 nm to above 100 nm. Figure S9a and S9b showed the DLS results of TPEDC nanoparticles and Ce6 nanoparticles with different average hydrodynamic diameter sizes, respectively. Therefore, we presented a facile and general strategy to prepare pure organic nanoparticles with well controlled sizes.

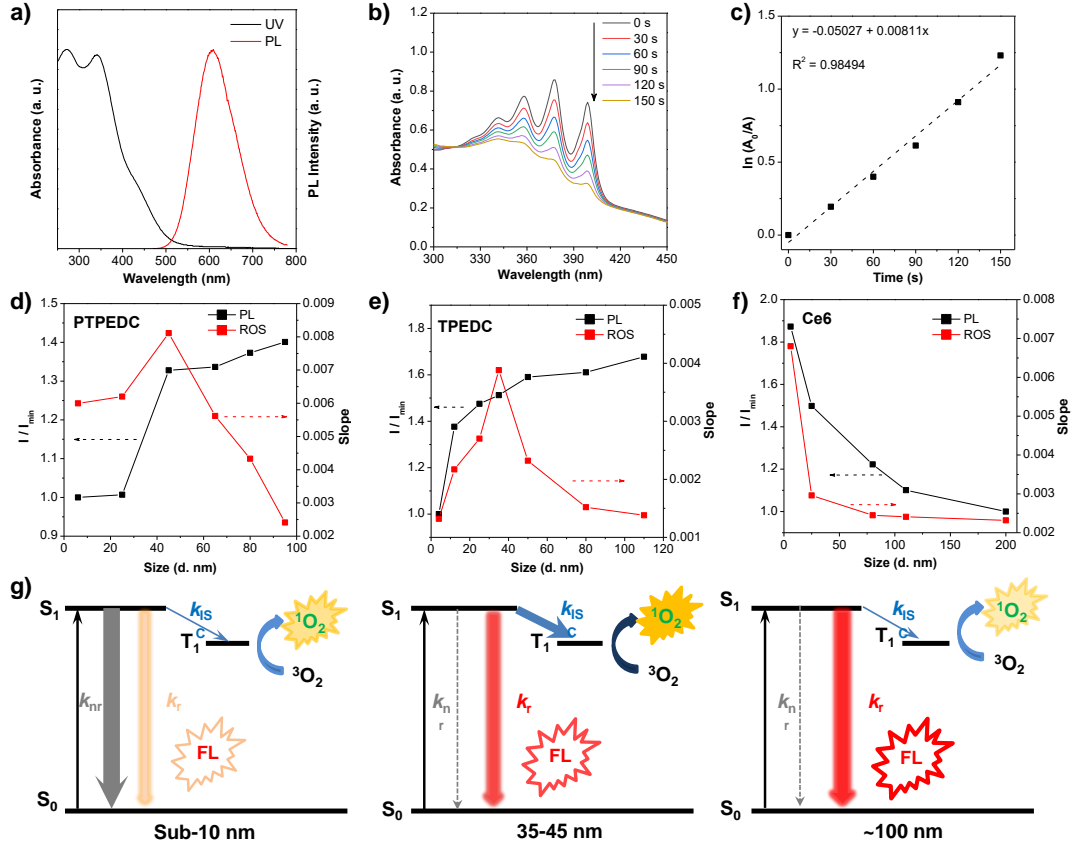**2.3 Size-dependent fluorescence and ROS production**

Figure 3. (a) UV and PL spectra of 45 nm PTPEDC nanoparticles. (b) Absorption spectra of 45 nm PTPEDC nanoparticles in the presence of ABDA under light irradiation. (c) ABDA degradation rate in (b), where A_0 and A are the absorbance of ABDA at 399 nm before and after light irradiation. PL intensity and ROS production efficiencies of PTPEDC (d), TPEDC (e) and Ce6 (f) nanoparticles along with increased nanoparticle sizes (I_{min} is emission intensity of nanoparticles with minimal particle sizes, and I is the emission intensity with varied NP sizes, the ABDA degradation slope of $\ln(A_0/A)$ represents ROS generation efficiency). (g) The Jablonski diagram showing the non-radiative, radiative, and intersystem cross (ISC) processes of AIE nanoparticles with different sizes. S_0: ground state, S_1: lowest excited singlet state, T_1: lowest excited triplet state, FL: fluorescence. k_{nr}, k_r and k_{ISC} are the rate constants of non-radiative relaxation, radiative dissipation, and ISC processes, respectively.

The propeller structures of AIEgens could non-radiatively dissipate excited energy via intramolecular motions, while restriction of intramolecular motions in aggregate blocks such energy deactivation process and redirects the excited energy dissipation via the radiative-decay and ISC processes. Therefore, AIEgens as a novel class of fluorophores possess the unique advantage of "the more aggregated, the brighter the fluorescence". To evaluate the size effect on the photophysical properties, we have used the same AIEgen concentration in all the following experiments and PTPEDC nanoparticles were firstly studied (Figure 3). All the PTPEDC nanoparticles showed the same absorption and emission maxima at 339 nm and 609 nm, respectively (Figure 3a). As compared to PTPEDC aggregates in water (or PTPEDC molecules in THF), PTPEDC nanoparticles showed similar absorption and emission spectra.

To reasonably evaluate the size effect, the brightness of these different sized nanoparticles was compared under the same PTPEDC concentration. Figure S10a showed the different fluorescence emission of PTPEDC nanoparticles of different sizes. When the size of PTPEDC nanoparticles increased from sub-10 nm to ~100 nm, the fluorescence of the nanoparticles increased by 40%. The results showed that the enhanced fluorescence emission of PTPEDC nanoparticles with the increased size.

(9,10-Anthracenediyl-bis(methylene)-dimalonic acid (ABDA) which reacts with $^1O_2$ and forms the corresponding endoperoxide with largely reduced absorbance was selected as the $^1O_2$ indicator to test the $^1O_2$ production ability of these PTPEDC nanoparticles. ABDA in the presence of PTPEDC nanoparticles showed gradually decreased absorbance from 300 to 450 nm under light irradiation, indicating the generation of $^1O_2$ (Figure 3b and 3c). ABDA itself under light irradiation showed negligible absorbance decrease, which confirmed the origin of $^1O_2$ from PTPEDC nanoparticles (Figure S10b). The effect of nanoparticle sizes on $^1O_2$ generation efficiency was further evaluated. Figures 3d and S10c-h show the ABDA decomposition rates in relationship to PTPEDC nanoparticle sizes, under the same PTPEDC concentration. The ROS generation efficiency of PTPEDC nanoparticles increased first and then decreased along with increasing nanoparticle sizes, which reached best ROS production efficiency at the size of 45 nm. The photophysical properties including fluorescence quantum yields, radiation transition rate (K_F), ISC rate (K_{ISC}) etc. are summarized in Table 1. The results showed that increasing nanoparticle sizes could increase both fluorescence quantum yields and K_F (K_F (25 nm) < K_F (45 nm) < K_F (80 nm)), while the K_{ISC} follows the order of K_{ISC} (80 nm) < K_{ISC} (25 nm) < K_{ISC} (45 nm), in consistence with ROS generation efficiency results. Taking together, both the fluorescence intensity and ROS generation ability of PTPEDC nanoparticles increased when the size was increased from 6 nm to 45 nm, while the fluorescence was continuously enhanced as the expense of ROS generation ability when further increasing the nanoparticle sizes.

Similar trends were also observed for TPEDC nanoparticles (Figures 3e and S11), where the best ROS production performance was obtained for 35 nm TPEDC nanoparticles. The difference is that TPEDC nanoparticles showed a higher fluorescence enhancement factor when the sizes increased from 4 nm to 110 nm, as well as a lower $^1O_2$ enhancement factor in the size ranging of 4 to 35 nm. The reason should be attributed to the conjugated polymeric nature of PTPEDC which possess a higher hydrophobicity, and hence a higher aggregation degree at small nanoparticle sizes. In addition, PTPEDC nanoparticles showed better ROS production over TPEDC nanoparticles at all tested sizes, further indicating that polymerization could enhance ISC process and increase ROS production. However, the situation is quite different for Ce6 nanoparticles. As shown in Figures 3f and S12, Ce6 nanoparticles exhibited reduced fluorescence and $^1O_2$ upon increasing nanoparticle sizes, making it less suitable for

nanoengineering. The reason should be caused by the planar nature of Ce6, which tends to form strong π-π stacking interactions in aggregates, leading to notorious ACQ effects. We further compared the $^1O_2$ production efficiency of PTPEDC nanoparticles and commercial Ce6 nanoparticles with the same size under hypoxia condition. As shown in Figure S13, PTPEDC nanoparticles show a much faster ABDA decomposition ability over Ce6 nanoparticles under N_2 atmosphere, clearly suggesting the merits of AIE nanoparticles for PDT. In addition, we herein aim to provide a size-tuning strategy to improve ROS generation, which could also be applied to other AIE photosensitizers with much improved ROS generation efficiency, which could further improve the final PDT effect.

As for AIE photosensitizers, they have propeller structures with intramolecular rotors, which could dissipate excited energy *via* non-radiative pathways when AIE photosensitizers are loosely packed. When the nanoparticle size is small (from sub-10 nm to about 35-45 nm), excited energy dissipation pathways are dominated by the competition between nonradiative decay and fluorescence/ROS production. In this size range, increasing nanoparticle sizes will inhibit non-radiative dissipation, resulting in synchronically enhanced fluorescence and ROS production (Figure 3g). The non-radiative decay process has already been largely inhibited at sizes of 35 to 45 nm. The competition between fluorescence and ROS production dominates the excited energy relaxation when further increasing nanoparticle sizes. Larger nanoparticle sizes with higher degree of aggregation results in further enhanced brightness, which will inevitably lead to the reduced ISC process, finally resulting in the lower ROS production. Hence, the size of AIE nanoparticles in PDT should be around 35-45 nm to achieve the highest photodynamic effect. It has been widely reported that the energy dissipation rates of different processes after photosensitizers absorb photons are largely dependent on their aggregate state.[41, 42] However, these reports have underestimated the competition between fluorescence and ROS generation. Hence, our study provides new insight for further improving ROS generation by suppressing radiative decay process.

Table 1. Photophysical data of PTPEDC nanoparticles with the sizes of 25 nm, 45 nm and 80 nm.

Nanoparticle Size	Abs. (nm)	Em (nm)	$<\tau>$ (ns)	Φ_{PL} (%)	Φ_{ROS}[1] ($\times 10^{-3}$ s^{-1})	K_F ($\times 10^7$ s^{-1})	K_{ISC} ($\times 10^8$ s^{-1})
25 nm	340	608	7.92	5.2	6.20	0.96	1.71
45 nm	341	609	8.03	5.4	8.11	1.41	2.02
80 nm	341	609	8.95	8.3	4.33	1.44	1.19

[1] Φ_{ROS}, ROS generation efficiency is defined as the ABDA decomposition slope of $\ln(A_0/A)$, where A_0 and A are the absorbance of ABDA at 399 nm before and after light irradiation.

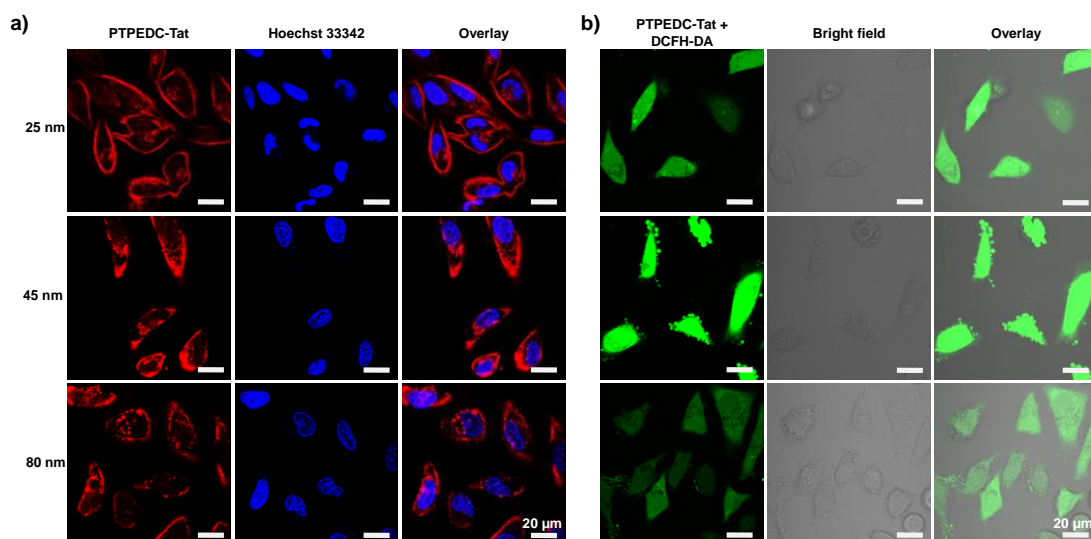## 2.4 Size-dependent cellular uptake and PDT

Figure 4. (a) Confocal images of HeLa cells after incubation with 25, 45, 80 nm PTPEDC-Tat nanoparticles at 10 μg/mL for 6 h. The nuclei were stained with Hoechst 33342 (1 μg/mL, 20 min) to provide blue emission. All the images share the same scale bar of 20 μm. (b) Confocal images of Hela cells to show intracellular ROS generation. Hela cancer cells were incubated with 25nm, 45 nm and 80 nm PTPEDC-Tat nanoparticles (5 μg/mL) for 4 h and DCFH-DA (40 μM) for 30 min in sequence, and the confocal images were acquired after light irradiation. All the images share the same scale bar of 20 μm.

The physical parameters of nanoparticles determine their biological fate, such as cellular uptake, cell toxicity, etc. Among them, size is one of the important factors affecting cellular uptake, which modulates the uptake efficiency and mechanism of nanoparticles.[43] However, previous studies are mainly based on inorganic ones such as quantum dots[44] or gold nanoparticles[45, 46], while less has been studied for pure organic nanoparticles. As organic nanoparticles possess different elasticity and surface softness, these findings based on inorganic nanoparticles might not be applicable for organic nanoparticles.[47] To further explore and evaluate the size impact of AIE nanoparticles in cellular uptake and PDT, PTPEDC nanoparticles were further selected for following cellular experiments. Using DSPE-PEG$_{2000}$ and DSPE-PEG$_{2000}$-Mal (mass ratio of 1:1) as the common matrices, maleimide-functionalized PTPEDC nanoparticles with size of 25 nm, 45 nm, and 80 nm were successfully synthesized. The cell membrane penetration peptide Tat (RKKRRQRRRC) was modified on their surface *via* thiol-maleimide click reaction to improve the cellular internalization efficiency of the obtained PTPEDC-Tat nanoparticles. Tat conjugation leads to slightly increased nanoparticle sizes, which are increased by 3-5 nm (Figure S14), suggesting that Tat modification will not significantly affect the sizes of these AIE nanoparticles (<10% variation). In addition, the conjugated Tat amounts in these nanoparticle solutions are determined to be 0.426, 0.485 and 0.508 mg/mL for 25, 45, 80 nm PTPEDC-Tat nanoparticles, respectively, based on the same PTPEDC concentration (1 mg/mL) (Figure S15 and Table S1). Increasing nanoparticle size leads to slightly increased Tat on nanoparticle surface, which shall be caused by the increased

surface volume for larger nanoparticles where PEG chains have more space to be extended into aqueous phase rather than being wrapped.

Herein, HeLa cancer cells were used as a model to evaluate the size-dependent cellular uptake and PDT effect of PTPEDC-Tat nanoparticles. HeLa cancer cells were incubated with PTPEDC-Tat nanoparticles (10 μg/mL and 20 μg/mL) at the size of 25 nm, 45 nm and 80 nm for 6 h, respectively, and then stained with the nuclear dye Hoechst 33342 (1 μg/mL) for 30 min. A confocal laser scanning microscope (CLSM) was used to obtain the fluorescence images as shown in Figures 4a and S17. The strong red fluorescence on HeLa cells confirmed the cellular internalization of PTPEDC-Tat nanoparticles. Comparison of cellular brightness reveals a higher cellular uptake for 45 nm sized nanoparticles over 25 nm and 80 nm sized ones (Figure S16). In addition, the redistribution of 45 nm sized nanoparticles ranged from cell surface to cell cytoplasm, while the majority of 25 nm and 80 nm PTPEDC-Tat nanoparticles was found on cell membrane. Hence, it demonstrated that organic nanoparticles with size around 45 nm have the highest cellular uptake performance. As internalization of nanoparticles into cells largely relies on binding capability of transmembrane peptides with proteins on cell membrane surface and membrane wrapping time.[44] Smaller nanoparticles possess a lower bind avidity, which tend to dissociate from cell membrane before being engulfed into cells.[48, 49] While larger nanoparticles with enhanced multivalent binding sites reduce the membrane motions and hence limit membrane wrapping process for nanoparticle internalization. Therefore, our data suggest that ~45 nm is the optimal size for cellular internalization, which shall be attributed to the balance between multivalent binding capability and membrane wrapping.

To evaluate the intracellular ROS generation, the HeLa cancer cells that have been labeled with PTPEDC-Tat nanoparticles at the size of 25 nm, 45 nm and 80 nm respectively were incubated with 2′,7′-dichlorodihydrofluorescein diacetate (DCFH-DA, a reactive oxygen species indicator) for a further 30 minutes, and then irradiated with white light (20 mW/cm^2) for 5 minutes. For the control groups receiving PTPEDC nanoparticles or light only, there is negligible green fluorescence inside HeLa cells, indicating poor intracellular ROS generation (Figure S18). However, bright green fluorescence from DCFH-DA was obtained for HeLa cells treated with PTPEDC-Tat nanoparticles and light, suggesting efficient intracellular ROS generation from PTPEDC-Tat nanoparticles (Figure 4b). PTPEDC-Tat nanoparticles at the size of 45 nm showed the brightest green fluorescence, followed by the size of 25 nm and 80 nm. The results confirmed the effective ROS production of PTPEDC-Tat nanoparticles in cells, and also verified that PTPEDC-Tat nanoparticles at the size of 45 nm had the strongest ROS production ability inside cells.
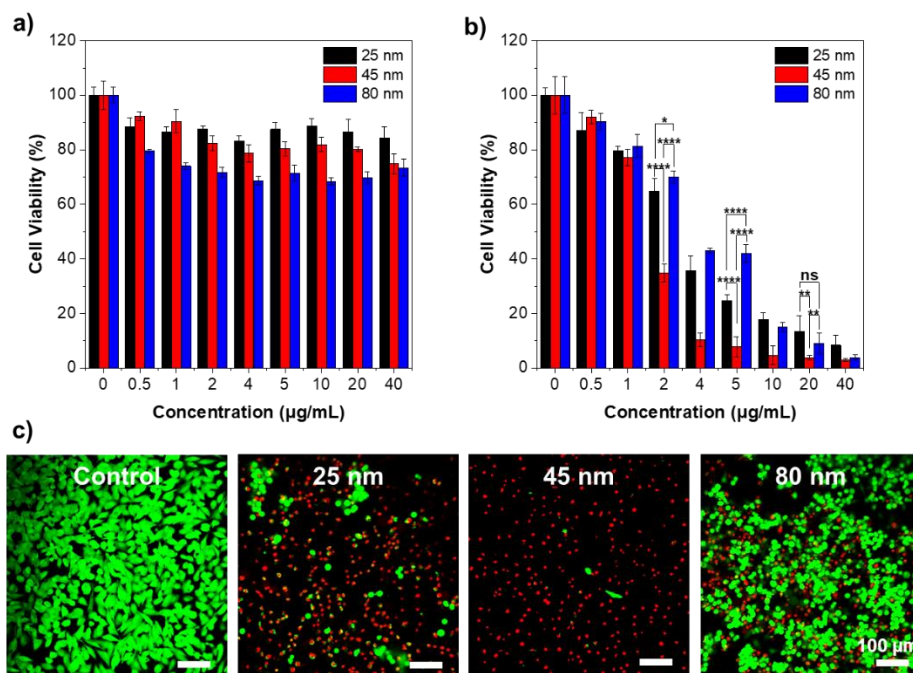
Figure 5. Cell viabilities of PTPEDC-Tat nanoparticles with the size of 25 nm, 45 nm and 80 nm treated HeLa cancer cells without (a) or with (b) white light irradiation (20 mW/cm², 5 min). Data presented means ± standard deviation (SD), $n = 6$. *$p < 0.05$, **$p < 0.01$, ****$p < 0.0001$. (c) Live/dead staining of PTPEDC-Tat nanoparticles with the size of 25 nm, 45 nm and 80 nm treated HeLa cancer cells with light irradiation (20 mW/cm², 5 min). The live cells were stained by Calcein AM (green, 2 μg/mL for 30 min), whereas dead cells were stained by propidium iodide (PI) (red, 6 μg/mL for 30 min). All the images share the same scale bar of 100 μm.

The killing effect of PTPEDC-Tat nanoparticles with different sizes (25 nm, 45 nm and 80 nm) on HeLa cancer cells by photodynamic treatment was further evaluated by standard MTT assay. PTPEDC-Tat nanoparticles showed very low dark toxicity to HeLa cancer cells (Figure 5a), indicating that PTPEDC-Tat nanoparticles have excellent biocompatibility in the dark. However, when PDT was applied, a significant difference in cell viability was observed. HeLa cancer cells were incubated with 25 nm, 45 nm and 80 nm PTPEDC-Tat nanoparticles for 4 hours, and then irradiated with white light (20 mW/cm²) for 5 minutes. The cell viability decreased sharply with the increased the incubation concentrations (based on AIEgen concentration). PTPEDC-Tat nanoparticles with different sizes showed significantly different cell viability (Figure 5b). At the concentration of 5 μg/mL, PTPEDC-Tat nanoparticles at the size of 25 nm, 45 nm and 80 nm have a killing effect on more than 75%, 90%, 60% of cells, respectively. The half-maximal inhibitory concentrations (IC$_{50}$) were calculated to be 2.72, 1.61, 3.63 μg/mL for 25 nm, 45 nm, and 80 nm PTPEDC nanoparticles, respectively. Hence, 45 nm PTPEDC-Tat nanoparticles with the highest ROS generation and best cellular uptake showed the best photodynamic cancer ablation performance. The calcein AM (live cell green) and propidium iodide PI (dead cell red) for live/dead staining was also applied to directly visualize the PDT effect of PTPEDC-Tat nanoparticles on HeLa cells (Figure 5c). After photodynamic

treatment, the three sizes of PTPEDC-Tat nanoparticles treated HeLa cells showed different portions of red and green emissive cells. The results of 45 nm PTPEDC-Tat nanoparticles showed almost all red fluorescent cells, 25 nm PTPEDC nanoparticles showed about 30 % of green emissive cells and 70 % of red emissive cells, and 80 nm PTPEDC nanoparticles showed about half of red fluorescent cells. The results revealed that HeLa cells can be effectively killed by PTPEDC-Tat nanoparticles under light irradiation, and 45 nm PTPEDC-Tat nanoparticles have the best photodynamic killing effect, contributed by the highest ROS generation efficiency and best cellular uptake performance. It should be noted that photodynamic induced cell death depends on many factors, where amount and location of these photosensitizers are virtually important factors apart from their ROS generation efficiency.[50, 51] In our work, changing nanoparticle sizes will automatically affect their cellular uptake and intracellular location, and it is nearly possible to perform a reasonable comparison on one factor while ruling out others. Our results suggested the highest cellular uptake and the strongest ROS production for 45 nm PTPEDC nanoparticles, making them the best candidate for photodynamic cancer cell ablation.

2.5 Size-dependent penetration depth and PDT in 3D multicellular spheroids
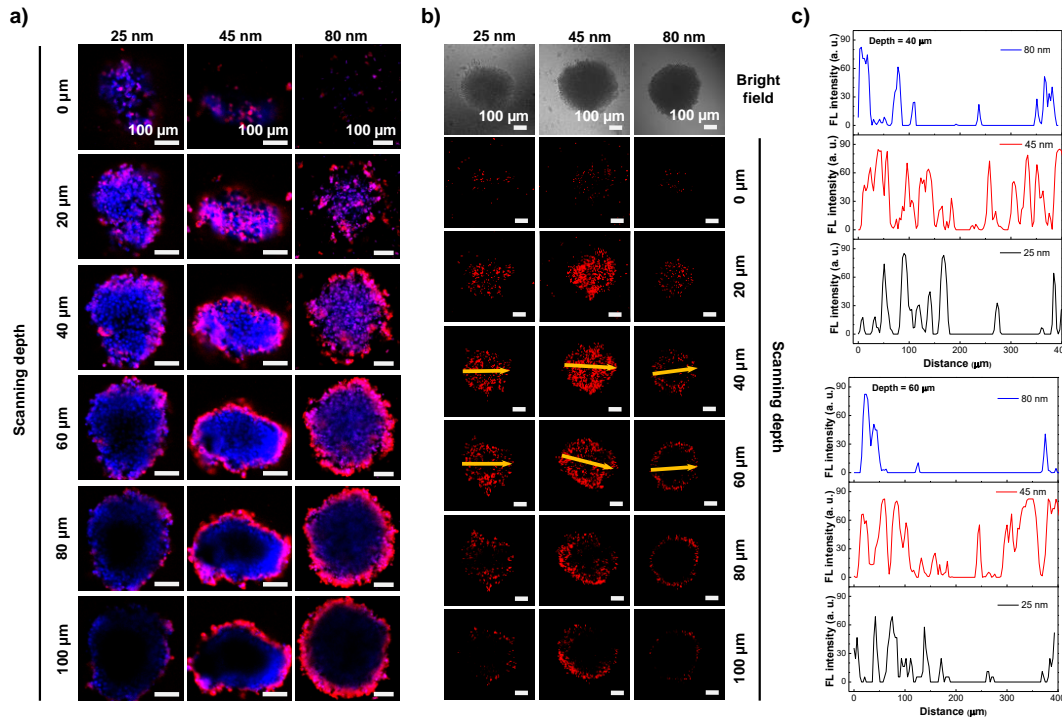

Figure 6. (a) Confocal images of 3D spheroids at different depths after treating with 25 nm, 45 nm and 80 nm PTPEDC-Tat nanoparticles (20 μg/mL) for 6 hours. The nuclei were stained with Hoechst 33342 (1.5 μg/mL, 1 h) to provide blue emission. (b) Confocal images of 3D spheroids labelled with PI to show dead cells in red. These cell spheroids were treated with 25 nm, 45 nm and 80 nm PTPEDC-Tat nanoparticles (20 μg/mL) for 6 hours, followed with light irradiation. The spheroids were stained with PI (red, 6 μg/mL for 1.5 h). (c) The corresponding fluorescent intensity histograms of 3D HeLa spheroids at the depth of 40 μm and 60 μm. All the images share the same scale bar of 100 μm.

The above results confirm that PTPEDC-Tat nanoparticles of different sizes have different intracellular uptake effects and photodynamic killing efficiency in a monolayer cell culture system. To further evaluate the tumor penetration ability and PDT performance of these nanoparticles, a 3D multicellular tumor spheroid model from HeLa cells was established. Confocal microscopy was used to study the fluorescence and penetration of 25 nm, 45 nm and 80 nm PTPEDC-Tat nanoparticles in these 3D cell spheroids (Figure 6a). It was found that all these nanoparticles were able to stain the superficial cells, while their ability to label interior cells reduced along with increased spheroid depths. Further analysis showed that the 45 nm PTPEDC-Tat nanoparticles still could label cells in the middle of 3D cell spheroid at a depth of 40-60 μm and the distribution of labelled cells was significantly more than that of nanoparticles with sizes of 25 nm and 80 nm. At deeper depths of 60-100 μm, 45 nm and 80 nm PTPEDC-Tat nanoparticles showed bright red light on the periphery of the 3D cell spheroid, while 25 nm PTPEDC-Tat nanoparticles showed a smaller amount of faint red light on the periphery of the 3D cell spheroid. Collectively, it indicated that the 45 nm PTPEDC-Tat nanoparticles showed the best penetration depth in the 3D spheroid. It should be noted that such conclusion is drawn based on the fluorescence brightness originated from PTPEDC-Tat nanoparticles, and the penetration ability of 25 nm nanoparticles might be underestimated as they have relative low fluorescence brightness.

To further verify the PDT performance in 3D multicellular spheroids, these spheroids treated with 25 nm, 45 nm and 80 nm PTPEDC-Tat nanoparticles were irradiated with white light for 5 minutes and further cultured for 12 hours to allow cell apoptosis and death progresses, and then stained with PI to show red fluorescence for dead cells. As shown in Figure 6b, 45 nm PTPEDC-Tat nanoparticles have the largest number of dead cells in the 3D cell spheroid in the depth ranging from 0-80 μm. Even at a depth of 80 μm, there were still many red cells in the center of the 3D cell spheroid. As for 25 nm PTPEDC-Tat nanoparticles, although there were dead cells inside the 3D cell spheroid at a depth of 60 μm, their numbers were significant less than that of 3D cell spheroid treated with 45 nm PTPEDC-Tat nanoparticles at the same depth (Figure 6c). On the other hand, 80 nm PTPEDC-Tat nanoparticles could only ablate these superficial cells located at the shell of the 3D spheroid under PDT treatment. These results further verified that the 45 nm PTPEDC-Tat nanoparticles have the deepest penetration in the 3D cell spheroid and the best photodynamic killing effect to these deeply located cells inside 3D spheroids.

3. Conclusion

In conclusion, we developed a facile strategy for the modulation and preparation of a series of pure organic nanoparticles with controllable sizes ranging from sub-10 nm to over 100 nm and reported the optimized sizes of AIE nanoparticles for efficient PDT. Such strategy is applicable to all tested fluorophores, including small organic dyes and semiconducting

polymers with planar or twisted molecular structures. When Ce6 nanoparticles showed reduced brightness and ROS generation efficiency along with nanoparticle size increasing, AIE nanoparticles showed simultaneously enhanced the fluorescence and ROS production efficiency upon increasing particle size from sub-10 nm to 35-45 nm, while further increasing sizes promoted nanoparticle brightness as expense of ROS generation. Our study further revealed that the optimal size ranges of AIE nanoparticles for PDT is around 45 nm, which not only possessed the best ROS production efficiency but also showed the highest cellular uptake, resulting in the most efficient photodynamic cell ablation performance. Furthermore, ~45 nm sized AIE nanoparticles also showed the best PDT killing effects to these deeply located cancer cells in the 3D multicellular spheroid model. Such study not only manifests the advantages of AIE PSs for phototheranostic nanoparticle engineering, but also delivers the optimal size ranging for efficient PDT. As the main contribution of this work, we have mainly focused on how nanoparticle size affects the ROS generation efficiency, while less *in vivo* exploration has been presented due to the short absorption and emission wavelengths of selected AIE photosensitizers in this work. Considering the rapid advances of organic optical agents especially PSs and nanoengineering technology for biological and biomedical applications, our discovery shall provide new windows to modulate the photophysical and biological behavior of these organic nanomaterials for improved theranostic performance, and we hope to present these findings in the near future.

Conflicts of interest

There are no conflicts of interest to declare.

Acknowledgments

Reference

[1]   P. Agostinis, K. Berg, K. A. Cengel, T. H. Foster, A. W. Girotti, S. O. Gollnick, S. M. Hahn, M. R. Hamblin, A. Juzeniene, D. Kessel, M. Korbelik, J. Moan, P. Mroz, D. Nowis, J. Piette, B. C. Wilson, J. Golab, *CA Cancer J. Clin.* **2011**, *61*, 250.

[2]   D. W. Felsher, *Nat. Rev. Cancer* **2003**, *3*, 375.

[3]   S. Su, W.-J. Wang, Q. Cao, H. Zhang, B. Liu, Y. Ling, X. Zhou, Z.-W Mao, *Angew. Chem. Int. Ed*. **2022**, *61*, e202115800.

[4]   J.-H. Liang, Y. Zheng, X.-W. Wu, C.-P. Tan, L.-N. Ji, Z.-W. Mao, *Adv. Sci.* **2020**, *7*, 1901922.

[5]   W. Fan, P. Huang, X. Chen, *Chem. Soc. Rev.* **2016**, *45*, 6488.

[6]   J. P. Celli, B. Q. Spring, I. Rizvi, C. L. Evans, K. S. Samkoe, S. Verma, B. W. Pogue, T. Hasan, *Chem. Rev.* **2010**, *110*, 2795.

[7]   S. S. Lucky, K. C. Soo, Y. Zhang, *Chem. Rev.* **2015**, *115*, 1990.

[8]   D. K. Chatterjee, L. S. Fong, Y. Zhang, *Adv. Drug Delivery Rev.* **2008**, *60*, 1627.

[9]   X. Dai, T. Du, K. Han, *ACS Biomater. Sci. Eng.* **2019**, *5*, 6342.

[10]   M. Ethirajan, Y. Chen, P. Joshi, R. K. Pandey, *Chem. Soc. Rev.* **2011**, *40*, 340.

[11]   S. Fulda, L. Galluzzi, G. Kroemer, *Nat. Rev. Drug Discov.* **2010**, *9*, 447.

[12]   B. M. Barth, E. I. Altinoğlu, S. S. Shanmugavelandy, J. M. Kaiser, D. Crespo-Gonzalez, N. A. DiVittore, C. McGovern, T. M. Goff, N. R. Keasey, J. H. Adair, T. P. Loughran, D. F. Claxton, M. Kester, *ACS Nano* **2011**, *5*, 5325.

[13]   J. Zhao, K. Xu, W. Yang, Z. Wang, F. Zhong, *Chem. Soc. Rev.* **2015**, *44*, 8904.

[14]   M. Guo, H. Mao, Y. Li, A. Zhu, H. He, H. Yang, Y. Wang, X. Tian, C. Ge, Q. Peng, X. Wang, X. Yang, X. Chen, G. Liu, H. Chen, *Biomaterials* **2014**, *35*, 4656.

[15]   S. Singh, A. Aggarwal, N. V. Bhupathiraju, G. Arianna, K. Tiwari, C. M. Drain, *Chem. Rev.* **2015**, *115*, 10261.

[16]   K. Li, B. Liu, *Chem. Soc. Rev.* **2014**, *43*, 6570.

[17]   A. Reisch, A. S. Klymchenko, *Small* **2016**, *12*, 1968.

[18]   W. Mao, Y. Liao, D. Ma, *Chem. Commun.* **2020**, *56*, 4192.

[19]   J. Tian, L. Xia, J. Wu, B. Huang, H. Cao, W. Zhang, *ACS Appl. Mater. Interfaces* **2020**, *12*, 32352.

[20]   G. Feng, B. Liu, *Acc. Chem. Res.* **2018**, *51*, 1404.

[21]   J. Luo, Z. Xie, J. W. Lam, L. Cheng, H. Chen, C. Qiu, H. S. Kwok, X. Zhan, Y. Liu, D. Zhu, B. Z. Tang, *Chem. Commun.* **2001**, 1740.

[22]   B. Ren, K. Li, Z. Liu, G. Liu, H. Wang, *J. Mater. Chem. B* **2020**, *8*, 10754.

[23]   Y. Hong, J. W. Y. Lam, B. Z. Tang, *Chem. Soc. Rev.* **2011**, *40*, 5361.

[24]   J. Mei, Y. Hong, J. W. Lam, A. Qin, Y. Tang, B. Z. Tang, *Adv. Mater.* **2014**, *26*, 5429.

[25]   J. Mei, N. L. Leung, R. T. Kwok, J. W. Lam, B. Z. Tang, *Chem. Rev.* **2015**, *115*, 11718.

[26]   X. Wu, J. Wu, J. Dai, B. Chen, Z. Chen, S. Wang, F. Wu, X. Lou, F. Xia, *Natl. Sci. Rev.* **2021**, 8, nwaa306.

[27]   J. Dai, Y. Li, Z. Long, R. Jiang, Z. Zhuang, Z. Wang, Z. Zhao, X. Lou, F. Xia, B. Z. Tang, *ACS Nano* **2020**, *14*, 854.

[28]   W. Wu, G. Feng, S. Xu, B. Liu, *Macromolecules* **2016**, *49*, 5017.

[29]   S. Xu, W. Wu, X. Cai, C. J. Zhang, Y. Yuan, J. Liang, G. Feng, P. Manghnani, B. Liu, *Chem. Commun.* **2017**, *53*, 8727.

[30]   J. Dai, X. Dong, Q. Wang, X. Lou, F. Xia, S. Wang, *Adv. Healthcare Mater.* **2021**, 2101036.

[31]   W. Wu, D. Mao, S. Xu, Kenry, F. Hu, X. Li, D. Kong, B. Liu, *Chem* **2018**, *4*, 1937.

[32]   G. Yang, J.-S. Ni, Y. Li, M. Zha, Y. Tu, K. Li, *Angew. Chem. Int. Ed.* **2021**, *60*, 5386.

[33].   J. Dai, X. Wu, S. Ding, X. Lou, F. Xia, S. Wang, Y. Hong, *J. Med. Chem.* **2020**, *63*, 1996.

[34]   F. Hu, S. Xu, B. Liu, *Adv. Mater.* **2018**, *30*, 1801350.

[35]   W. Liu, J. Zhang, Z. Zhou, D. Zhang, Y. Zhang, S. Xu, X. Zhu, *Adv. Mater.*, **2018**, *30*, 1800403.

[36] G. Feng, W. Wu, S. Xu, B. Liu, *ACS Appl. Mater. Interfaces* **2016**, *8*, 21193.

[37] N. T. K. Thanh, N. Maclean, S. Mahiddine, *Chem. Rev.* **2014**, *114*, 7610.

[38] E. Middha, P. N. Manghnani, D. Z. L. Ng, H. Chen, S. A. Khan, B. Liu, *Mater. Chem. Front.* **2019**, *3*, 1375.

[39] E. Lepeltier, C. Bourgaux, P. Couvreur, *Adv. Drug Deliv. Rev.*, **2014**, *71*, 86.

[40] S. Wang, J. Liu, G. Feng, L. G. Ng, B. Liu, *Adv. Funct. Mater.* **2019**, *29*, 1808365.

[41] W. Hou, J. W. H. Lou, J. Bu, E. Chang, L. Ding, M. Valic, H. H. Jeon, D. M. CHarron, C. Cloolens, D. Cui, J. Chen, G. Zhang, *Angew. Chem., Int. Ed.* **2019**, *58*, 14974.

[42] X. Li, C. Kim, S. Lee, D. Lee, H.-M. Chung, G. Kim, S.-H. Heo, C. Kim, K.-S. Hong, J. Yoon, *J. Am. Chem. Soc.* **2**017, *139*, 10880.

[43] J. Zhu, L. Liao, L. Zhu, P. Zhang, K. Guo, J. Kong, C. Ji, B. Liu, *Talanta* **2013**, *107*, 408.

[44] Z. Popovic, W. Liu, V. P. Chauhan, J. Lee, C. Wong, A. B. Greytak, N. Insin, D. G. Nocera, D. Fukumura, R. K. Jain, M. G. Bawendi, *Angew. Chem. Int. Ed.* **2010**, *49*, 8649.

[45] B. D. Chithrani, A. A. Ghazani, W. C. W. Chan, *Nano Lett*. **2006**, *6*, 662.

[46] W. Jiang, B. Y. Kim, J. T. Rutka, W. C. Chan, *Nat. Nanotech*. **2008**, *3*, 145.

[47] P. Gu, B. Chen, T. Zhai, Q. Li, X. Zuo, L. Wang, A. Qin, Y. Zhou, J. Shen, *ACS. Appl. Mater. Interfaces* **2021**, *13*, 19660.

[48] F. Osaki, T. Kanamori, S. Sando, T. Sera, Y. Aoyama, *J. Am. Chem. Soc*. **2004**, *126*, 6520.

[49] H. Gao, W. Shi, L. B. Freund, *Proc. Natl. Acad. Sci. USA* **2005**, *102*, 9469.

[50] W.-H. Chen, G.-F. Luo, X.-Z. Zhang, *Adv. Mater.* **2019**, *31*, 1802725.

[51] R. Wang, X. Li, J. Yoon, *ACS Appl. Mater. Interfaces* **2021**, *13*, 19543.

Table of Contents
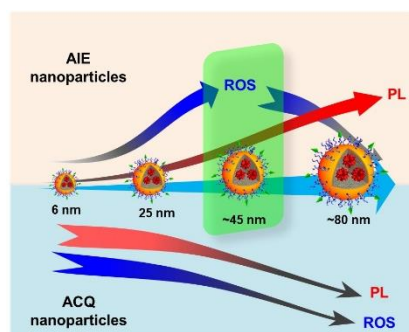
The photodynamic cancer cell ablation efficacy of photosensitizer-loaded nanoparticles is size dependent. The optimal size of AIE nanoparticle for photodynamic cancer cell ablation is around 45 nm, which show highest ROS generation efficiency, best cellular internalization, deepest penetration depth. Such study shall provide new windows for nanoengineering approach to improve photodynamic therapy performance.